Biogeosciences, 14, 1721–1737, 2017
www.biogeosciences.net/14/1721/2017/
doi:10.5194/bg-14-1721-2017

Biogeosciences Open Access EGU

Geochemical and microstructural characterisation of two species of cool-water bivalves (*Fulvia tenuicostata* and *Soletellina biradiata*) from Western Australia

Liza M. Roger[1,2], Annette D. George[1], Jeremy Shaw[2], Robert D. Hart[2], Malcolm Roberts[2], Thomas Becker[2,3], Bradley J. McDonald[4], and Noreen J. Evans[4]

[1]School of Earth Sciences, the University of Western Australia, Crawley 6009, Australia
[2]Centre for Microscopy, Characterisation and Analysis, the University of Western Australia, Crawley 6009, Australia
[3]Department of Chemistry, Nanochemistry Research Institute, Curtin University, GPO Box U1987, Perth 6845, Australia
[4]Department of Applied Geology, John de Laeter Centre, TIGeR, Curtin University, Bentley 6102, Australia

Correspondence to: Liza M. Roger (liza.roger@hotmail.fr, liza.roger@research.uwa.edu.au)

Received: 18 August 2016 – Discussion started: 13 January 2017
Revised: 13 March 2017 – Accepted: 13 March 2017 – Published: 31 March 2017

Abstract. The shells of two marine bivalve species (*Fulvia tenuicostata* and *Soletellina biradiata*) endemic to south Western Australia have been characterised using a combined crystallographic, spectroscopic and geochemical approach. Both species have been described previously as purely aragonitic; however, this study identified the presence of three phases, namely aragonite, calcite and Mg-calcite, using XRD analysis. Data obtained via confocal Raman spectroscopy, electron probe microanalysis and laser ablation inductively coupled plasma mass spectrometry (LA-ICP-MS) show correlations between Mg / S and Mg / P in *F. tenuicostata* and between Sr / S and S / Ba in *S. biradiata*. The composition of the organic macromolecules that constitute the shell organic matrix (i.e. the soluble phosphorus-dominated and/or insoluble sulfur-dominated fraction) influences the incorporation of Mg, Sr and Ba into the crystal lattice. Ionic substitution, particularly Ca^{2+} by Mg^{2+} in calcite in *F. tenuicostata*, appears to have been promoted by the combination of both S- and P-dominated organic macromolecules. The elemental composition of these two marine bivalve shells is species specific and influenced by many factors, such as crystallographic structure, organic macromolecule composition and environmental setting. In order to reliably use bivalve shells as proxies for paleoenvironmental reconstructions, both the organic and inorganic crystalline material need to be characterised to account for all influencing factors and accurately describe the "vital effect".

1 Introduction

As calcifiers, molluscs play an important role in the ocean carbonate cycle. The calcium carbonate formed by marine organisms is a complex geochemical source and sink of carbon, which controls total oceanic carbon content and pCO_2 (partial pressure of CO_2) and more generally contributes to ocean alkalinity (e.g. Gattuso and Hansson, 2011). The biomineralisation process or, more precisely, the elemental and isotopic composition of biogenic $CaCO_3$, is affected by physiological processes (e.g. Freitas et al., 2006; Gillikin et al., 2005b; Lowenstam and Weiner, 1989) and environmental conditions at the time of deposition (e.g. Ferguson et al., 2011; Gazeau et al., 2010; Hahn et al., 2014; Heinemann, 2011; Henkes et al., 2013; Lowenstam and Weiner, 1989; Schöne et al., 2011). Molluscs are globally distributed and demonstrate sequential growth, thus providing high-resolution seasonal and sub-seasonal records of environmental conditions (e.g. Jones and Quitmyer, 1996).

A number of bivalve species are extremely long lived, with lifetimes of many decades or even centuries, e.g. fresh water pearl mussels (e.g. Schöne et al., 2004), geoduck clams (e.g. Strom et al., 2004), ocean quahogs (e.g. Schöne et al., 2005) and giant clams (e.g. Ayling et al., 2006; Bonham, 1965). Many oceanic conditions, such as seawater surface temperature, productivity, circulation and carbon reservoir dynamics, have been reconstructed successfully using bivalve shell records (e.g. Klein et al., 1996; Lazareth et

al., 2003; Richardson et al., 2004; Wanamaker et al., 2011). However, an organism's physiological control on the chemical composition of its shell can affect the reliability of the parameters recorded (e.g. Gillikin et al., 2005b; Lazareth et al., 2013, 2003). Differences between the measured isotopic and the elemental composition in carbonate materials are typically attributed to a physiological or biological influence commonly called the "vital effect" (Zeebe et al., 2008). Spero et al. (1991) first attempted to describe the vital effect through the quantitative modelling of stable carbon isotopes in foraminifera. The influence of the vital effect is variable between species, which is problematic for the development of a unique geochemical equilibrium model for seawater property reconstructions.

The work of pioneers in the field of molluscan biomineralisation, Bowerbank (1844) and Carpenter (1845, 1847) amongst others, shifted the focus from fossil structures to "modern" biogenic $CaCO_3$ structures (such as coral skeleton and mollusc shells). Influential work by Urey et al. (1951) first used stable oxygen isotope values ($\delta^{18}O$) in biogenic $CaCO_3$ (belemnite rostrum) as a proxy for seasonal temperature change. Certain limitations remained, such as separating $\delta^{18}O_{water}$ (which is linearly correlated to salinity) from the temperature signals, leading to the development of other proxies according to their temperature dependency, e.g. Sr / Ca and Mg / Ca ratios (Gillikin et al., 2005a; Shirai et al., 2014). However, further work showed that elemental composition is strongly controlled by biological factors including growth rate (e.g. Gillikin et al., 2005b), calcification rate (e.g. Carré et al., 2006), ontogenetic age (e.g. Purton et al., 1999), organic matrix (e.g. Schöne et al., 2010; Takesue et al., 2008) and microstructure (overall fabrics) (e.g. Schöne et al., 2013; Shirai et al., 2014).

Long-term records of seawater parameters (e.g. temperature, alkalinity and pH) are essential for understanding past climatic and oceanic changes in the current context of global climate change. Data from diverse geographical locations are needed to develop a global understanding of those changes. Records from bivalve shells have contributed considerably to our knowledge, but environmental controls need to be well defined and differentiated from biological and physiological factors (e.g. Jacob et al., 2008).

This study focuses on the microstructure and composition of shells from two species of bivalves endemic to southwestern Australia to gain insight into the physio-chemical processes involved in molluscan shell calcification. It constitutes the first step towards monitoring global climate change through biogenic carbonate in southwestern Australia. In general, limited geochemical data are available for temperate Australian marine bivalves and, to our knowledge, this work is the first multimodal (crystallographic, spectroscopic and geochemical) study focusing on marine bivalve species from Australian waters. The structure and mineral composition of shells from the Western Australian bivalves *F. tenuicostata* and *S. biradiata* have not been previously investigated as a potential proxy for future studies using this integrated approach. Given the absence of corals along the southern coast of Western Australia and the south coast of Australia as a whole, bivalve shells could serve as an alternative proxy for generating records of historical ocean chemistry provided that the overarching mechanisms are well defined and understood (e.g. elemental equilibrium and the vital effect). This study contributes to the global understanding of how marine bivalves record environmental change through shell growth and the processes governing marine biogenic carbonate production.

2 Materials and methods

2.1 Study area and marine setting

Samples were collected from the muddy sands (600–800 µm grain size) of King George Sound at a depth of 3–5 m on the southern coast of Western Australia near the town of Albany (Fig. 1). This area experiences seasonal freshwater inputs, a temperate to Mediterranean climate, a mean annual rainfall of 931.5 ± 0.2 mm (between 1877 and 2014), a maximum of $\sim 126.1 \pm 0.2$ mm of rainfall in August and a minimum of $\sim 30.1 \pm 0.2$ mm in December (Australia Government Bureau of Meteorology; Brouwers et al., 2013; Klausmeyer and Shaw, 2009). The main currents influencing the area are the Capes Current (coastal current) flowing westward, the Leeuwin Current (shelf current) flowing eastward and the Flinders Current (oceanic current) flowing westward (Cresswell and Golding, 1980). Further south, Australian waters meet the cold and nutrient-rich Antarctic waters. The southwestern coastline of Australia is impacted by strong winter storms influenced by pressure systems over the Great Australian Bight, as well as the Leeuwin Current dynamics. Seawater surface temperatures (SST) vary annually between 16 and 21 °C (August–September to April–May) and bottom temperatures vary between 15 and 20.6 °C (Australian Government Bureau of Meteorology) at 40–50 m of maximum depth.

2.2 Species

The study uses two species of bivalves: *Fulvia tenuicostata* (Lamarck, 1819) (the "thin-ribbed cockle") and *Soletellina biradiata* (Wood, 1815) (the "double-rayed sunset clam"; Fig. 2). Both species are native and endemic to southwestern Australia (WoRMS, 2016). *F. tenuicostata* (Mollusca: Bivalvia: Veneroida: Cardiidae), shown in Fig. 2a and b, is typically 50–55 mm in length (anterior to posterior margin). The shells of this species are cream coloured, becoming yellow towards the margin (the periostracum can show staining from the surrounding mud). The shells are thin and delicate with narrow ribs (Fig. 2a and b). This genus is found in moderately sheltered areas of muddy sand (WoRMS, 2016). The shell structure of *F. tenuicostata* consists of a prismatic outer layer

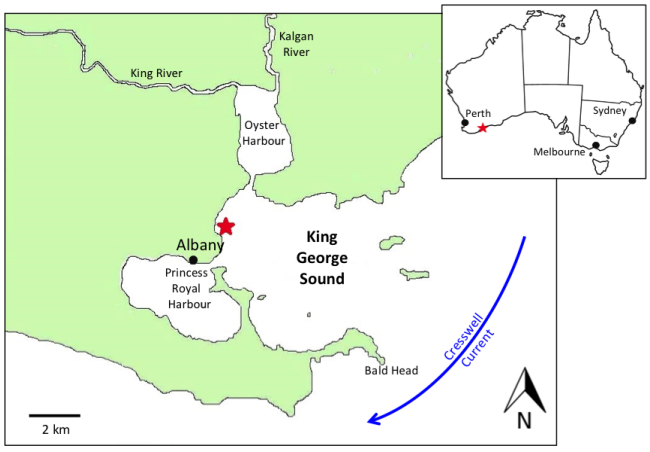

Figure 1. A map of King George Sound and the surrounding coastline in south Western Australia. The sampling site is indicated by the red star.

(OL), a simple crossed-lamellar middle layer (ML) and a complex crossed-lamellar inner layer (IL). *S. biradiata* (Mollusca: Bivalvia: Veneroida: Psammobiidae) shells, shown in Fig. 2c and d, may measure up to 70 mm. The shells are thin walled and have an elongated shape. With the thick periostracum removed, the shells are cream coloured with tinges of pink and purple and two distinctive pale radial rays extending from the umbo to the growing edge. *S. biradiata* is also found in moderately sheltered areas with muddy sand substrates. The shell structure of *S. biradiata* consists of a prismatic OL composed of acicular prismatic crystals directed toward the outer surface and locally curved, a simple crossed-lamellar ML and a complex crossed-lamellar IL. The OL may be absent, in which case the lamellae of the ML extend to the outer surface as noted for other species of this subfamily (Popov, 1986; Schneider and Carter, 2001).

2.3 Sample preparation

Shells (five *F. tenuicostata* and three *S. biradiata*) were rinsed with fresh water, manually cleaned of any organic residues by scrubbing, then soaked in sodium hypochlorite (12.3 vol%) for approximately 12 h. Shells were thoroughly rinsed with Milli-Q water (EMD Millipore Corporation, Darmstadt, Germany) and then air dried. According to Krause-Nehring et al. (2011), the treatment of biogenic calcium carbonate to remove organic matter may have an impact on the elemental and crystallographic composition in the bivalve *Arctica islandica*. The effects of sodium hypochlorite (NaOCl) pretreatment (also used in our study) on *A. islandica* shell powder were insignificant compared to other treatments tested in that study. Indeed, Sr / Ca and Mg / Ca ratios did not change significantly, and very little to no dissolution or phase change was observed. NaOCl treatment has also proved to be the most efficient method to remove organic matter with the least effect on structure and composition in coral cores (Nategaal et al., 2012). Krause-Nehring et al. (2011) performed their study on powdered, pre-cleaned shells (manual removal of the periostracum) and found very little effect. In our study, where intact shells were pretreated with NaOCl, we suggest that the geochemical and crystallographic composition of the bivalves studied here was not significantly altered despite having some hypochlorite solution percolate through.

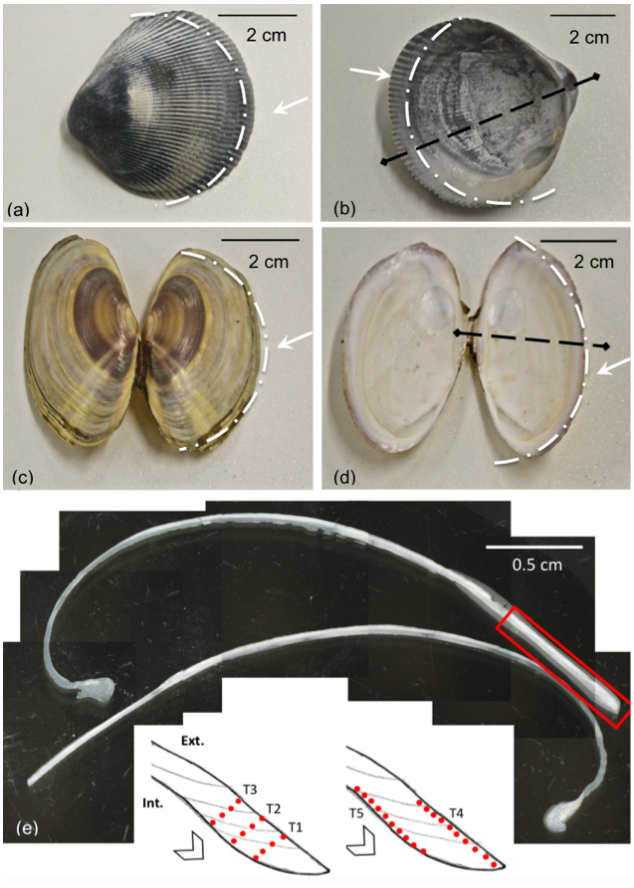

Figure 2. Photographs of the external (left) and internal (right) views of the bivalves *Fulvia tenuicostata* **(a, b)** and *Soletellina biradiata* **(c, d)**. **(e)** A photo mosaic showing the ventral margin (*S. biradiata*) as seen in a thin section. Powder was sampled from the ventral margin for X-ray diffraction analysis (the white dashed lines and arrows in **a, b, c** and **d**). The area adjacent to the ventral margin was then targeted for confocal Raman microscopy, LA-ICP-MS and EPMA (the red box in **e**). The lower panel shows a representation of the laser spots along five transects (T1–T5). T1–T3 are parallel to the shell edge, and T4 and T5 are parallel to the external and internal shell margin (respectively).

Shells were sampled along the growing edge using a handheld dental drill for X-ray diffraction analysis (Fig. 2). Fifty milligrams of very fine powder was mixed with ∼ 10 mg of CaF_2 (20 % by weight) and mounted on a low-level background holder according to the settings described in the Supplement S1. The bivalves were then cut along the axis of

maximum growth (from umbo to ventral margin), fixed in styrene polymer and mounted on a glass slide with EPOTEK 301 epoxy glue (Billerica, MA, USA). They were then trimmed and polished to a thickness of 20–40 µm. The thin-sectioned bivalves, thus prepared, were used for petrographic observations, confocal Raman spectroscopy and laser ablation mass spectrometry work. All the analyses described below targeted the ventral margin of the shells, which is the youngest material. The growth increments of *F. tenuicostata* are about twice those of *S. biradiata* at 1 and 0.5 mm, respectively. Each measurement was made to encapsulate approximately the same growth period.

2.4 X-ray diffraction analysis

X-ray diffraction (XRD) analysis of the powdered shells was performed using a PANalytical Empyrean diffractometer (Eindhoven, The Netherlands) operated at 40 kV and 40 mA (Cu $K\alpha$ radiation and Ni beta filter) and a PANalytical PIXcel position sensitive detector. The particular settings are described in the Supplement S1. A corundum NIST standard (676a; certificate number 382200) was used as a primary external standard and calcium fluoride (CaF_2) was used as a secondary internal standard. The amount of the secondary standard was tested by analysing different CaF_2 : sample ratios. Since no major differences were observed between the various ratios tested, a 20 % weight of CaF_2 was chosen. CaF_2 (lattice parameter $a = b = c = 5.4662(2)$ Å and $\alpha = \beta = \gamma = 90°$) is an ideal internal standard because its diffraction peaks do not interfere with those of $CaCO_3$.

The mineral phases were identified using the Inorganic Crystal Structure Database (ICSD) and the International Centre for Diffraction Data (ICDD). The Rietveld refinement technique was used to quantify the phases. The Scherrer equation (Cullity and Weymouth, 1957) was used to calculate the coherently scattering domain (CSD) size (i.e. crystallite size) using the dominant reflections of calcite (104) and aragonite (111). Both the Rietveld refinement and the Scherrer calculation were performed using the PANanlytical HighScore Plus software (version 3.0e). The non-crystalline fraction, or amorphous material, in the powder was typically calculated from the overestimation of the secondary standard during the Rietveld refinement (Scarlett and Madsen, 2006).

2.5 Confocal Raman microscopy

Confocal Raman microscopy (CRM) uses intense monochromatic light (here, an infrared laser) to irradiate samples. The subsequent molecular vibrations produce a highly specific Raman spectrum that reflects the molecular structure and the chemical identity of the samples. Changes in the intensity and peak position indicate different vibrational modes of a molecule and therefore may reveal subtle differences in the crystalline form, especially between the different polymorphs of $CaCO_3$ (Nehrke and Nouet, 2011). $CaCO_3$ peaks measured using CRM are caused by the unit cell symmetry of the crystals and the molecular carbonate ions (CO_3^{2-}). Because of their shared CO_3^{2-}-related vibrational modes, the differentiation between aragonite and calcite was accomplished using the lower end of the spectrum, 50 to 1200 cm^{-1}. In CRM, a spectroscopy system is coupled with a confocal microscope, allowing for the mapping of samples with chemical sensitivity.

CRM was undertaken on thin sections of bivalve shells to confirm XRD-determined mineral phases and to provide key information about the crystallographic structure of $CaCO_3$. To mitigate the high fluorescence levels caused by a green excitation laser (wavelength 532 nm), a diode infrared laser module (wavelength 785 nm) with 20 × objective and a 0.4 numerical aperture was used, coupled with the Raman imaging system (WITec, Ulm, Germany; alpha300 RA+). CRM was performed in reflection mode, whereby the scattered light is collected through a 100 µm detection fibre connected to a UHTS 300 spectrometer equipped with a 300 lines/mm grating. The full Raman spectra at each imaging pixel were acquired using a camera with a thermoelectrically cooled, back-illuminated CCD chip. The first-order Raman peak of silicon (520.2 cm^{-1}) was used to optimise the alignment and signal intensity before each analysis. Measurements were made as large area scans with the accumulation of three to five spectra to minimise error (± 1 cm^{-1}) and an integration time of 0.1 to 0.050 s. Two spectral ranges were measured: 0 to 1600 cm^{-1} and 1600 to 3000 cm^{-1}; the second range was explored in an attempt to detect organic functional groups (C−H or C=O) within the crystalline structures. The CRM data were processed and analysed with the WITec Project FOUR software.

2.6 Electron probe microanalysis

Quantitative chemical maps were acquired on petrographic thin sections using a JEOL 8530F HyperProbe (JEOL Solutions for Innovation, Peabody, MA, USA) equipped with five tuneable wavelength dispersive spectrometers. The operating conditions for the instrument calibration were comprised of a 40° take-off angle, a beam energy of 15 kV and a beam current of 20 nA. The beam was defocussed to 2 µm. The elements were acquired using analysing crystals: PET (pentaerythritol) for Ca $K\alpha$, S $K\alpha$ and Sr $l\alpha$; TAP (thallium acid phthalate) for Na $K\alpha$ and Mg $K\alpha$. The standards used for the instrument calibration were barite for S $K\alpha$, calcite for Ca $K\alpha$, celestite for Sr $l\alpha$, periclase for Mg $K\alpha$ and jadeite for Na $K\alpha$. Peak counting times were 20 s and mean atomic number background corrections were used throughout (Donovan and Tingle, 1996). The results are the average of three points and the detection limits ranged from 0.008 wt % for S $K\alpha$ to 0.010 wt % for Mg $K\alpha$ to 0.049 wt % for Sr $l\alpha$. The Armstrong–Love/Scott algorithm was used for data reduction (Armstrong, 1988). Quantitative element maps were obtained using the Probe Image® software (Probe

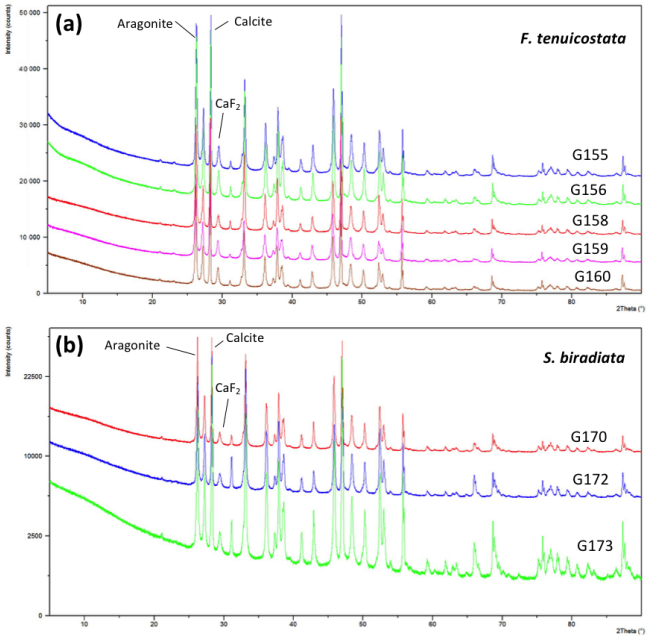

Figure 3. The X-ray diffraction patterns of specimens of *Fulvia tenuicostata* **(a)** and *Soletellina biradiata* **(b)**. Each XRD pattern is offset from the next (along the y axis) to show the consistency of the diffraction peak positions. The sample ID is indicated to the right of each diffraction pattern. Intensity is relative. Note: G154, G157 and G172 were not analysed using XRD because the sample weight was too low. The main diffraction peaks indicated for each phase identified aragonite, calcite and calcium fluorite CaF_2.

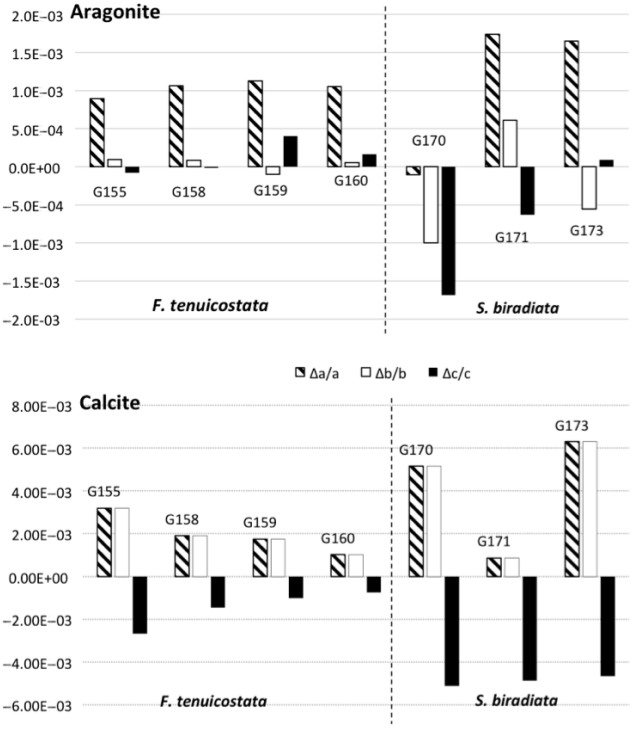

Figure 4. The aragonite lattice distortion presented as $\Delta a/a$, $\Delta b/b$ and $\Delta c/c$ compared to the mineral standard (Pokroy et al., 2006) for four specimens of *F. tenuicostata* and three of *S. biradiata*. The y axis indicates the amount of distortion compared to ICSD-98-015-7993 mentioned above. Negative distortions are indicative of shrinking, and positive distortions are indicative of stretching.

Software, Inc., Eugene, OR, USA) for X-ray intensity acquisition. The beam current was 80 nA with a 40 ms per pixel dwell time and a 4×4 µm pixel dimension. Image processing and quantification was performed off-line with the CalcImage® software (Probe Software, Inc.) and output to Surfer® (Golden Software, LLC, Golden, CO, USA).

2.7 Laser ablation ICP-MS

The analysis of carbonate material was undertaken using a Resonetics RESOlution M-50A-LR (Australian Scientific Instruments, Fyshwick, Australia) incorporating a Compex 102 excimer laser (Coherent Inc., Santa Clara, CA, USA) coupled with an Agilent (Santa Clara, CA, USA) 7700s quadrupole ICP-MS on shell material that had already been thin sectioned. Following two cleaning pulses and a 20 s period of background analysis, samples were spot ablated for 30 s at a 7 Hz repetition rate using a 75 µm beam and a laser energy of 5 J cm^{-2}. Oxide polyatomic interferences were minimised by tuning flow rates for a ThO / Th ratio of < 0.5 %. The sample cell was flushed with ultra-high-purity He (350 mL min^{-1}) and N_2 (3.8 mL min^{-1}), and high-purity Ar was employed as the plasma carrier gas. The international glass standard NIST 612 and the coral standard MACS-3 were used as the primary reference materials to calculate the elemental concentrations (using stoichiometric ^{43}Ca as the internal standard element) and to correct for instrument drift on all elements. Standard blocks were run after every 20th unknown sample. The mass spectra were reduced using iolite (Armstrong, 1988). Data were collected on a total of 16 elements measured as ^{7}Li, ^{24}Mg, ^{28}Si, ^{31}P, ^{34}S, ^{44}Ca, ^{52}Cr, ^{55}Mn, ^{56}Fe, ^{63}Cu, ^{66}Zn, ^{75}As, ^{88}Sr, ^{111}Cd, ^{138}Ba and ^{208}Pb. The Si concentration was used to determine if or when the laser hit the glass slide. The measurements taken when the laser hit the glass were discarded.

Trace element concentration profiles were measured in four shells of *F. tenuicostata* and two of *S. biradiata*. Five transects were measured on each shell: three parallel transects of seven to eight spots (T1–T3) oblique to the shell surface, one transect along the outer portion of the outer shell layer (T4; 10 spots) and one along the inner portion of the outer shell surface (T5; 10 spots; Fig. 2). Transects T1–T3 were measured to assess the elemental variation towards the inner shell surface and the potential thickness of the last growth layer deposited. T4 and T5 were measured to compare trace element concentrations in the innermost layer of the shell to the outermost layer.

Table 1. The lattice parameters a, b and c (Å) of aragonite after Rietveld refinement and other reference materials for comparison. *Perna canaliculus*: marine bivalve, *Acanthocardia tuberculata*: marine bivalve and *Strombus decorus persicus:* marine gastropod.

Origin		a	b	c
This study				
G156	biogenic: *Fulvia tenuicostata*	5.7471	4.9634	7.9673
G158	biogenic: *Fulvia tenuicostata*	5.7481	4.9634	7.9678
G159	biogenic: *Fulvia tenuicostata*	5.7484	4.9624	7.9712
G160	biogenic: *Fulvia tenuicostata*	5.7480	4.9632	7.9692
G170	biogenic: *Soletellina biradiata*	5.7413	4.9580	7.9545
G171	biogenic: *Soletellina biradiata*	5.7519	4.9660	7.9629
G173	biogenic: *Soletellina biradiata*	5.7514	4.9602	7.9686
Pokroy et al. (2007)[a]				
ICSD-98-015-7993	mineral: Morocco	5.7420	4.9630	7.9680
JCPDS-41-1475	mineral	5.7439	4.9623	7.9680
ICSD-98-015-7994	biogenic: *P. canaliculus*	5.7520	4.9670	7.9640
ICSD-98-015-7992	biogenic: *A. tuberculata*	5.7480	4.9650	7.9640
ICSD-98-015-7995	biogenic: *S. decorus persicus*	5.7530	4.9690	7.9590
ICSD-98-015-7996	biogenic: *S. decorus persicus* (bleached)	5.7430	4.9630	7.9640
ICSD-98-015-7997	biogenic: *S. decorus persicus* (annealed)	5.7530	4.9690	7.9610
De Villiers (1967)[b]				
ICSD-98-001-5194	mineral: Nevada	5.7400	4.9670	7.9670
Bragg (1925)[c]				
ICSD-98-005-6090	mineral: Hungary	5.7300	4.9500	7.9550
External standard				
NIST 676a alumina	synthetic powder	4.7593	4.7593	12.992
Internal standard				
CaF2	synthetic powder	5.4664	5.4664	5.4664

[a] JCPDS: data file 41-1475, Joint Committee on Powder Diffraction Standards. Keller, L., Rask, J. and Buseck, P., 1989. JCPDS card no. 41-1475, Arizona State Univ., Tempe, AZ, USA., ICDD Grant-in-Aid. [b] XRD from single crystal $CaCO_3$, Nevada. [c] XRD from single crystal $CaCO_3$, Hungary.

3 Results

3.1 Shell mineral composition

The XRD patterns indicate that the shells are composed of calcite and aragonite based on matching diffraction peaks (Fig. 3). The third identifiable diffraction pattern represents the internal standard, CaF_2 (20 % weight of the total sample). The Rietveld refinement was applied in order to obtain an accurate phase quantification for each sample; however, the values produced by the software corresponding to the weight ratio of CaF_2 added were lower than the actual amount. Consequently, the results are not considered useful. Quantification errors in XRD are commonly caused by residual moisture, large organic content, amorphous crystallites or, in this case, errors due to small sample sizes and insufficient particle size reduction (Scarlett and Madsen, 2006). In the present case, moisture, organic material and amorphous crystals could all cause an overestimation (Scarlett and Madsen, 2006), but the underestimation was likely caused by the small sample size (~ 50 mg). Accurate quantification on small sample sizes can be obtained by using synchrotron technology. Although the phases cannot be quantified, the lattice parameters and crystallite sizes (i.e. the coherently scattering domain or CSD) produced post-refinement and after the Scherrer calculation can be used because of the addition of the pre-calibrated CaF_2 standard.

All of the samples analysed were indexed to the orthorhombic symmetry system for aragonite and the hexagonal system for calcite. The lattice parameters (a, b, c) generated by the Rietveld refinement differ from the geological reference materials for both calcite and aragonite (Table 1). All samples of *F. tenuicostata* manifest expansion in aragonite and calcite along the a axis (Fig. 4). All samples of *S. biradiata*, except one (G170), show the same phenomenon. In contrast, G170 shows contraction along all axes. The b axis in both phases and both species also generally shows a positive distortion (stretching) with a few exceptions (*F. tenuicostata*, G159; *S. biradiata*, G170 and G173; all three in aragonite only). The calcite c axis shows shrink-

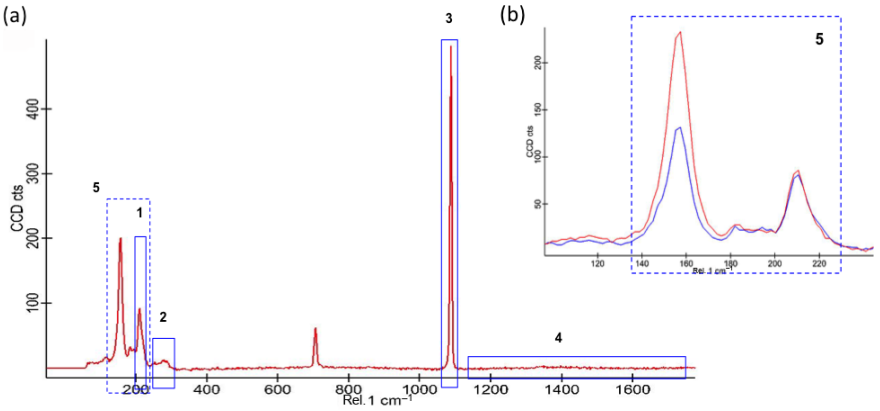

Figure 5. The typical Raman spectra from *S. biradiata* and *F. tenuicostata* **(a)**. The blue boxes correspond to the filters applied to the data: filter 1 (Σ peak area) centred at 209 cm^{-1} (width = 36.6 cm^{-1}), filter 2 (Σ peak area) centred at 282 cm^{-1} (width = 66.3 cm^{-1}), filter 3 (centre of mass, weighted width) centred at 1085 cm^{-1} (width = 36.6 cm^{-1}) and filter 4 (Σ peak area) centred at 1450 cm^{-1} (width = 600 cm^{-1}). The blue dashed box, filter 5, encapsulates filter 1 and a filter centred at 152 cm^{-1} (Σ peak area, width = 36.6 cm^{-1}) to represent their calculated peak intensity ratio. The blue and red spectra **(b)** show the peak intensity difference seen at 152 and 209 cm^{-1}. Each filter measures the peak area, except filter 3, which measures the full width at half maximum and produces a qualitative map. Filter 1 targeted the aragonitic phase, and filter 2 targeted calcite. Filter 3, by measuring variation in FWHM, represents crystallinity and crystallite order. Filter 4, by targeting the tail of the spectrum, shows fluorescence, since the peaks related to organics tend to show best in the tail of the spectrum. And finally, the peak intensity ratios (filter 5) show changes in the crystallite orientation (aragonite crystallites).

ing in both species. The distortion along the *c* axis in aragonite is variable (two out of four *F. tenuicostata* show contraction and two out of three for *S. biradiata*). The largest distortion was found in calcite, particularly for *a* and *b* (+0.12 to +0.02 %); *c* only shows small distortions of −0.03 to −0.004 %. Aragonite is distorted along the *a* axis between +0.03 and +0.017 %; the *b* and *c* axes manifest smaller distortions of +0.014 and −0.008 % at a maximum, respectively. The main difference between the two species considered here lies in the amount of distortion, whereby *F. tenuicostata* manifests a smaller distortion compared to *S. biradiata* (Fig. 4). The maximum distortion in aragonite is 0.02 %. It is 0.066 % in calcite for *F. tenuicostata* (both $\Delta a/a$) and 0.03 and ∼ 0.13 %, respectively, in *S. biradiata* (also $\Delta a/a$). Furthermore, although minimal, *F. tenuicostata* shows generalised stretching (0.004 % maximum) along the *c* axis in aragonite, whereas *S. biradiata* shows shrinking (−0.008 % maximum).

The CSD sizes estimated using the Scherrer equation (with $K = 0.9$) for the four dominant aragonite diffraction peaks corresponding to reflections (111), (102), (201) and (122) reveal aragonite crystals ranging from ∼ 34 to ∼ 144 nm long (Table 2). The majority of the CSD values fall in the nanocrystal category (< 100 nm), but some, especially those for the (122) plane, belong to the larger ultra-fine category (100–500 nm). The CSD sizes estimated for calcite used one dominant diffraction peak corresponding to reflection (104) to reveal smaller crystallites than in aragonite (∼ 23 to ∼ 29 nm long).

Different phases in the samples were identified using a combination of lattice modes and internal modes. Calcite and aragonite can be identified using the librational modes L_c (282 cm^{-1}) and L_a (209 cm^{-1}), respectively, and the in-plane band v_4 (713 cm^{-1} for calcite and 702, 706 and 717 cm^{-1} for aragonite); the shared peaks (translational mode, *T*, ∼ 152 cm^{-1} and symmetry stretch, v_1, 1085 cm^{-1}) represent the CO_3^{2-} ion motion and the C−O bond stretching common to both $CaCO_3$ polymorphs (Cuif et al., 2012, Fig. 5). Although very small and broad compared to aragonite-specific peaks, only the L_c peak identified

Table 2. The aragonite and calcite crystallite size (coherently scattering domain, or CSD) in nm, estimated using the Scherrer equation (Cullity and Weymouth, 1957) with $K = 0.9$ on four main diffraction peaks of aragonite and the peak (104) of calcite.

Sample ID	CSD (nm)				
	Aragonite peak (hkl)				Calcite peak (hkl)
	(111)	(102)	(201)	(122)	(104)
F. tenuicostata					
G155	68.5	58.8	41.6	105.2	25.5
G156	64.2	69.9	–	58.3	26.2
G158	69.1	64.4	42.3	–	28.3
G159	45.6	50.1	35.6	34.4	29.1
G160	66.3	73.0	–	–	26.2
S. biradiata					
G170	69.1	68.1	51.2	–	29.0
G171	111.7	72.3	37.2	143.8	23.3
G173	93.7	93.9	46.8	99.1	24.6

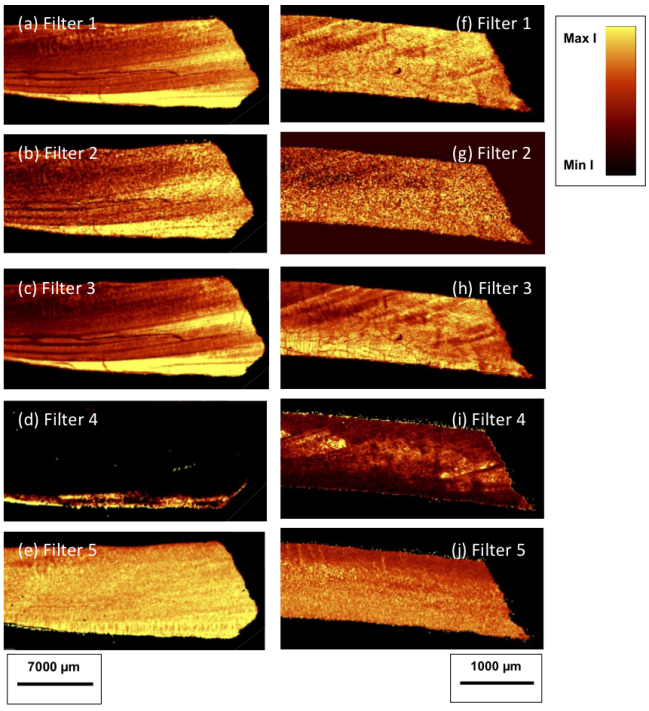

Figure 6. Images extracted from the filters applied to the Raman spectra (see Fig. 5) from samples G171 (*S. biradiata*) **(a–e)** and G155 (*F. tenuicostata*) **(f–j)**. Scale bar: 7000 µm **(a–e)** and 1000 µm **(f–j)**. Colour scale: the bright colours correspond to high intensities (high CCD counts) and the dark colours correspond to low intensities (low CCD counts). The sub-horizontal and curved lines, most visible in **(a–c)** and **(f–h)**, are structural features of the shells. Scale bar: 500 µm.

calcite. The most pronounced aragonite peak is L_a. The scan range of the spectrometer was increased to 3000 cm^{-1} in order to detect the potential presence of organic compounds (e.g. Nehrke and Nouet, 2011); however, no features characteristic of these groups were found. As a consequence, the spectra presented here only extend to 2000 cm^{-1}.

Four filters were applied to each Raman spectrum (Fig. 5) to highlight different phases or reveal particular features of the shell: (1) Σ peak area of aragonite (centred at 209 cm^{-1}); (2) Σ peak area of calcite (centred at 282 cm^{-1}); (3) centre of mass and weighted width (full width at half maximum) of v_1 (centred at 1085 cm^{-1}); and (4) Σ peak area of the tail of the spectrum targeting fluorescence (centred at 1450 cm^{-1}). Peak intensities at 152 cm^{-1} (translational mode T) and 209 cm^{-1} were also ratioed (PIR) to distinguish the crystal orientation variations (Figs. 5 and 6).

Aragonite and calcite were both found in all samples analysed using CRM. The small intensity of the calcite peak indicates that it is a minor phase. Two distinct types of spectra are visible for aragonite (Fig. 5), both with identical peak positions but different peak intensity ratios (PIR) (Figs. 5, 6e and j) between the translational mode T and the other peaks characteristic of aragonite (filter 5, Figs. 5 and 6).

The full width at half maximum (FWHM) of the symmetric stretch $v_1(CaCO_3^{2-})$ reveals sequential variations or, more precisely, alternating high and low peak widths, especially in sample G154 (Fig. 6c and h). The other samples show more discrete changes in FWHM. Filter 4 (the filter showing fluorescence) reveals clear banding throughout the samples (Fig. 6e and j).

Table 3. The EPMA detection limits (3σ) on bivalve samples. The Mg and Sr contents in both *S. biradiata* and *F. tenuicostata* were below the limits of detection (see Figs. 8 and 9).

Element (symbol)	*Fulvia tenuicostata*	*Soletellina biradiata*
Sodium (Na)	0.1355	0.17
Magnesium (Mg)	0.102	0.127
Sulfur (S)	0.01	0.085
Calcium (Ca)	0.115	0.1425
Strontium (Sr)	0.47	0.595

3.2 Elemental composition

The EPMA results show that the total elemental compositions are consistently between 98 and 100 wt % (Figs. 7a and 8a). Calcium is generally consistent across the samples with an average concentration of ∼ 39.5 wt % (Figs. 8b, 9b). S and Na comprise up to 0.16 and 0.66 wt %, respectively, but importantly show variations in concentration with opposing trends; i.e. high Na corresponds to low S and vice versa (Fig. 6). The concentrations of S and Na correspond to growth lines with overall Na content higher towards the external surface of the shell and S towards the internal surface. Low S and high Na correspond to higher fluorescence levels detected using CRM (1450 cm^{-1} filter; Fig. 6d and i). These results are consistent for both *S. biradiata* (Fig. 7) and *F. tenuicostata* (Fig. 8). Ca is typically uniformly distributed throughout each shell; nevertheless, the patterns revealed by CRM correspond to the patterns on the Ca distribution maps. The patterns revealed by filters 4 and 5 (crystallinity and crystal orientation, respectively), when applied to the Raman spectrum, correspond to those visible on the Ca wt % map. Mg and Sr are below the instrumental detection limit (Table 3) and are not presented here.

The trace element concentration profiles measured using LA-ICP-MS showed that the NIST160 and MACS standard reproducibility is in the range of acceptable values (between 0.5 and 4 % on most elements; Supplement S2). Very little reproducibility was observed between T1, T2 and T3 (Figs. 9 and 10) for all six shells tested; however, compositionally distinct layers were identified, as were differences between species (Figs. 11 and S3). In *F. tenuicostata*, the ratios of Sr / Ca, S / Ca and Pb / Ca along transects T1–T3 generally increase from the external sur-

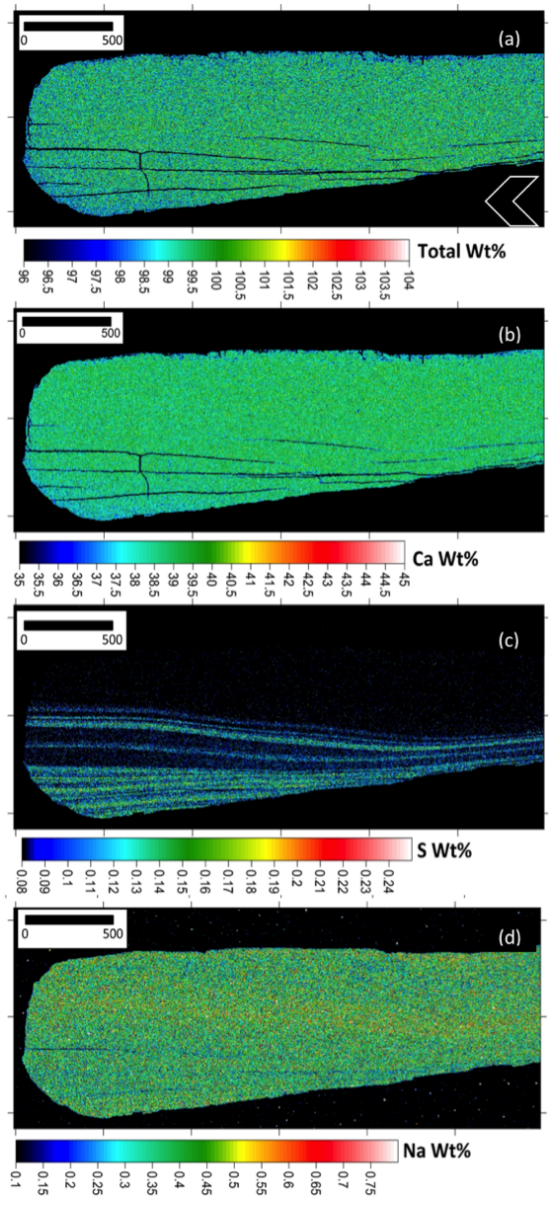

Figure 7. The EPMA elemental map of sample G171, *S. biradiata*, for totals **(a)**, Ca concentration **(b)**, S concentration **(c)** and Na concentration **(d)**. The Mg and Sr concentrations were below the instrumental detection limit and are therefore not presented here. The arrow **(a)** indicates the direction of growth. Note: this shell shows a thick edge compared to the adjacent shell section. The *S. biradiata* shell thickness is variable along the cross section.

face inwards (maximum $+1\,\mathrm{mmol\,mol^{-1}}$, $+3\,\mathrm{mmol\,mol^{-1}}$ and $+0.05\,\mu\mathrm{mol\,mol^{-1}}$, respectively; Supplement S3). Only Sr / Ca in G158 decreases by $2\,\mathrm{mmol\,mol^{-1}}$ inwards (Supplement S3). Mg / Ca, P / Ca and Ba / Ca (Figs. 11 and S3) follow the opposite trend, with a maximum decrease of $1.5\,\mathrm{mmol\,mol^{-1}}$, $0.06\,\mathrm{mmol\,mol^{-1}}$ and $3\,\mu\mathrm{mol\,mol^{-1}}$, respectively. The elemental ratios in *S. biradiata* all decrease along the T1–T3 transects from the outer to the inner layer ($\mathrm{Mg/Ca}$ $-0.15\,\mathrm{mmol\,mol^{-1}}$, $\mathrm{P/Ca}$ $-0.04\,\mathrm{mmol\,mol^{-1}}$, $\mathrm{Li/Ca}$ $-4\,\mu\mathrm{mol\,mol^{-1}}$, $\mathrm{Ba/Ca}$ $-2\,\mu\mathrm{mol\,mol^{-1}}$), except $\mathrm{Pb/Ca}$ ($+0.06\,\mu\mathrm{mol\,mol^{-1}}$) and S / Ca, which is relatively stable at $1.3\,\mathrm{mmol\,mol^{-1}}$. Sr / Ca increases inwards ($+1.5\,\mathrm{mmol\,mol^{-1}}$) but decreases to its original level at the edge of the internal layer ($\sim 2\,\mathrm{mmol\,mol^{-1}}$). Li, Ca, Mn and Ba concentrations in *F. tenuicostata* are not linearly correlated to the other trace elements measured, but a statistically significant (paired t test) linear correlation was found between [P] / [Sr] ($R^2 = 0.70$, $p < 2.2 \times 10^{-16}$), [P] / [S] ($R^2 = 0.74$, $p < 2.2 \times 10^{-16}$), [P] / [Mg] ($R^2 = 0.55$, $p = 1.283 \times 10^{-7}$) and [S] / [Mg] ($R^2 = 0.55$, $p < 2.2 \times 10^{-16}$). Li, Mg, Ca and Mn in *S. biradiata* are not linearly correlated to the other trace elements measured, but a statistically significant (paired t test) linear correlation was found between [Sr] / [S] ($R^2 = 0.74$, $p < 2.2 \times 10^{-16}$), [Sr] / [Pb] ($R^2 = 0.60$, $p < 2.2 \times 10^{-16}$), [Sr] / [Ba] ($R^2 = 0.92$, $p < 2.2 \times 10^{-16}$), [Ba] / [S] ($R^2 = 0.66$, $p < 2.2 \times 10^{-16}$) and [Ba] / [Pb] ($R^2 = 0.55$, $p < 2.2 \times 10^{-16}$).

T4–T5 measurements confirm the compositional differences between the external and internal layers (Figs. 12 and S3). Overall, the external layer of the *S. biradiata* shells studied demonstrates higher ratios of Li / Ca, Mg / Ca, P / Ca, Sr / Ca and Ba / Ca compared to the internal layer. Only S / Ca and Pb / Ca do not follow this pattern, where S / Ca is the same in both layers and Pb / Ca is higher in the internal layer (Figs. 12 and S3). In comparison, *F. tenuicostata* shells show higher ratios of Mg / Ca, Sr / Ca, S / Ca, Ba / Ca and Pb / Ca in their internal layer compared to their external layer. P / Ca decreases inwards and Li / Ca is essentially consistent.

S and P are indicators of organic content, and their presence in the bivalves reflects a variation in macromolecule content throughout the shells. *F. tenuicostata* has a higher S-containing macromolecule content in the organic matrix of its internal layer, whereas a higher P / Ca ratio in the outer layer suggests that the organic matrix is richer in P-containing macromolecules in that section of the shell. The shells of *S. biradiata* are visibly more complex. They also show high S / Ca and low P / Ca towards the innermost layer, but for most of the shell, variable S / Ca and P / Ca ratios suggest that the external layers are characterised by alternating P- and S-containing macromolecules in organic components (Figs. 7–8 and 10–11).

4 Discussion

4.1 Mineralogy and microstructure

Although *S. biradiata* and *F. tenuicostata* belong to subfamilies typically described as aragonitic (Schneider and Carter, 2001), the XRD analysis and CRM results reveal a dominant aragonitic composition and a minor calcite fraction. The Rietveld refinement did not allow for the quantification

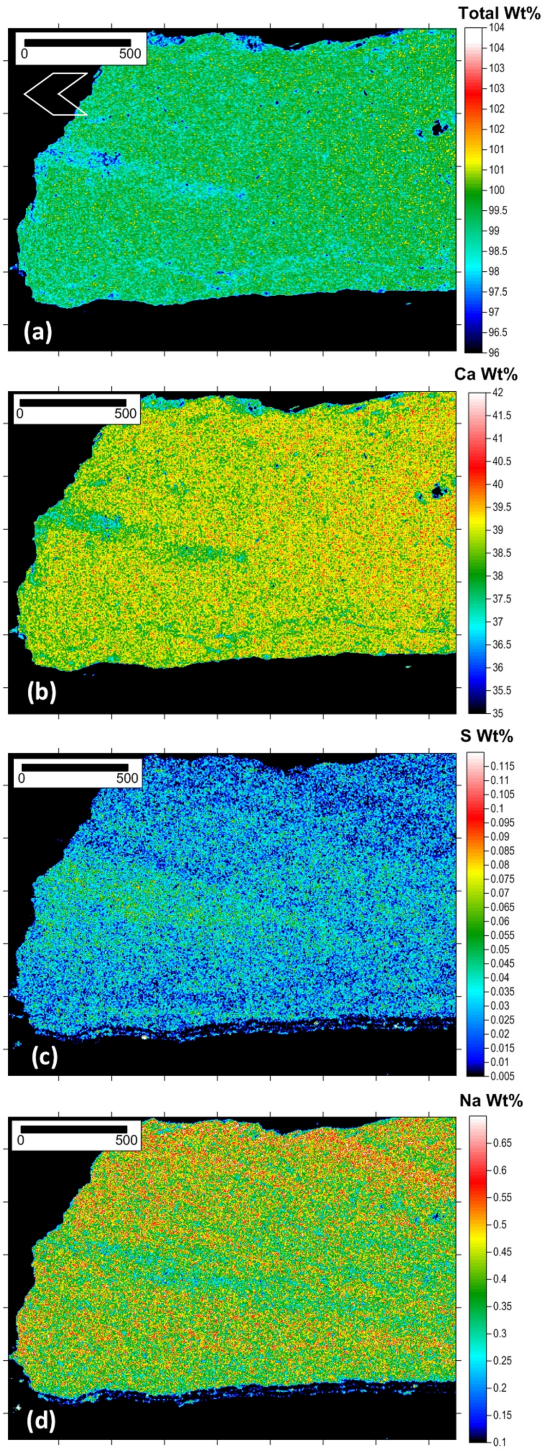

Figure 8. The EPMA elemental map of sample G155, *F. tenuicostata*, for totals **(a)**, Ca concentration **(b)**, S concentration **(c)** and Na concentration **(d)**. Mg and Sr were below the instrumental detection limit and are therefore not presented. The dashed line indicates scan overlap, since the sample was scanned twice to optimise precision and quality. Scale bar: 500 µm. The arrow indicates the direction of growth.

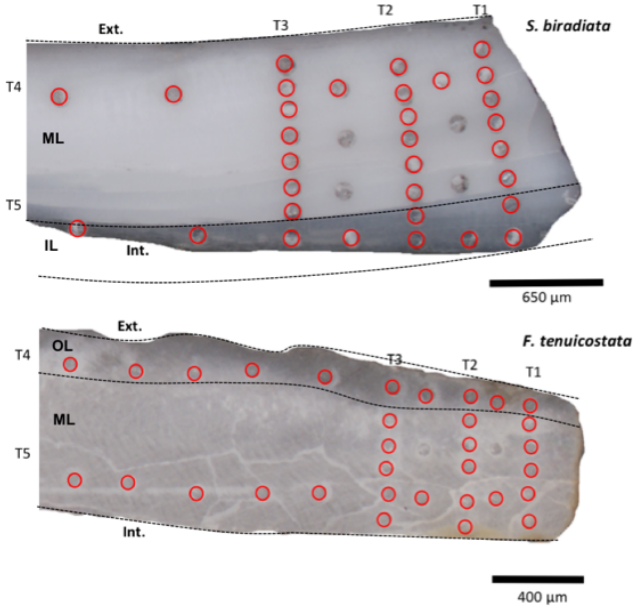

Figure 9. The location of the laser spots along the five transects. T1–T3 transect towards the inner shell surface and parallel to each other. T4 transects along the outer portion of the outer shell layer and T5 along the inner portion of the outer shell layer. The inner and outer portions of the outer shell layer are indicated by "Int." and "Ext.", respectively. The shell layers are indicated by OL for the outer layer, ML for the middle layer and IL for the internal layer. Note the absence of the outer shell layer and the inner shell layer in these sections of *S. biradiata* and *F. tenuicostata*, respectively. T4 and T5 were sampled from different shell layers as labelled.

of the different phases; however, CRM confirmed the presence of calcite by measuring small intensities of the calcite librational mode L_c compared to that of aragonite L_a. The Raman spectra of *S. biradiata* have a slightly more intense calcite peak at 282 cm^{-1} in comparison to *F. tenuicostata*, and the XRD pattern shows that the main calcite peak in *F. tenuicostata* is generally sharper and offset towards 30° 2θ compared to that of *S. biradiata*. According to Schroeder et al. (1969), this peak shift is indicative of the presence of Mg in carbonate, which suggests that some Mg^{2+} ions have beeb substituted for Ca^{2+} in the $CaCO_3$ crystal lattice in *F. tenuicostata*. Considering the preferential incorporation of Mg^{2+} into calcite as opposed to aragonite (Mucci and Morse, 1982), we conclude that although both species appear to have similar amounts of calcite incorporated within their aragonitic shell, in *F. tenuicostata*, Ca^{2+} ions have been partially substituted by Mg^{2+} in the calcite lattice. This is not the case in *S. biradiata*. Sample G170 (*S. biradiata*), which shows shrinking in its aragonite phase according to the XRD results, has a negative peak shift (CRM) indicative of Sr^{2+} substitution in aragonite. The LA-ICP-MS analysis of G170 was not undertaken because the thin section was too cracked towards the ventral margin; therefore, the higher Sr / Ca in G170 is assumed from the distortion measurements and CRM.

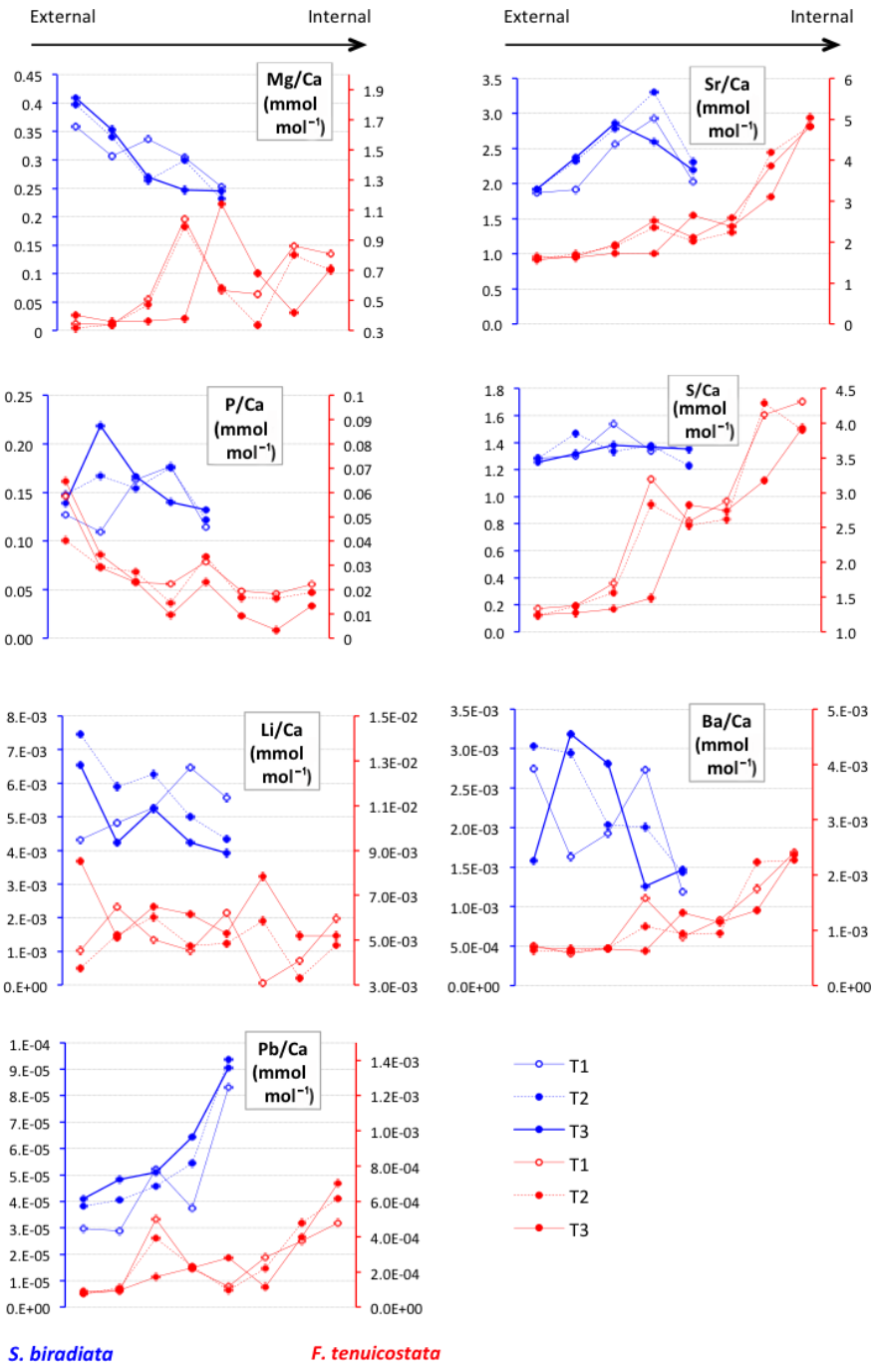

Figure 10. The LA-ICP-MS results for transects T1, T2 and T3. The blue lines represent the results for *S. biradiata* (G171) and the red lines represent the results for *F. tenuicostata* (G155). The five laser spots or transects were done on *S.biradiata.*

Aragonite is present in two different orientations in most of the *F. tenuicostata* samples. The combination of these two orientations (e.g. Fig. 6) clearly corresponds to the crossed-lamellar microstructure characteristic of many bivalve shells. The microstructure of *S. biradiata* shells consists of a prismatic outer shell layer, a crossed-lamellar middle layer and a complex crossed-lamellar inner layer (not present in the portion of the shell in Fig. 6). Both species precipitate their shells differently from a structural point of view. The precipitation of microstructural units in a crossed-lamellar pattern is complex. The structural complexity of *F. tenuicostata*, with its crossed-lamellar pattern associated with marked ribs, suggests a higher level of biological control on $CaCO_3$ precipitation, which may influence the overall elemental composi-

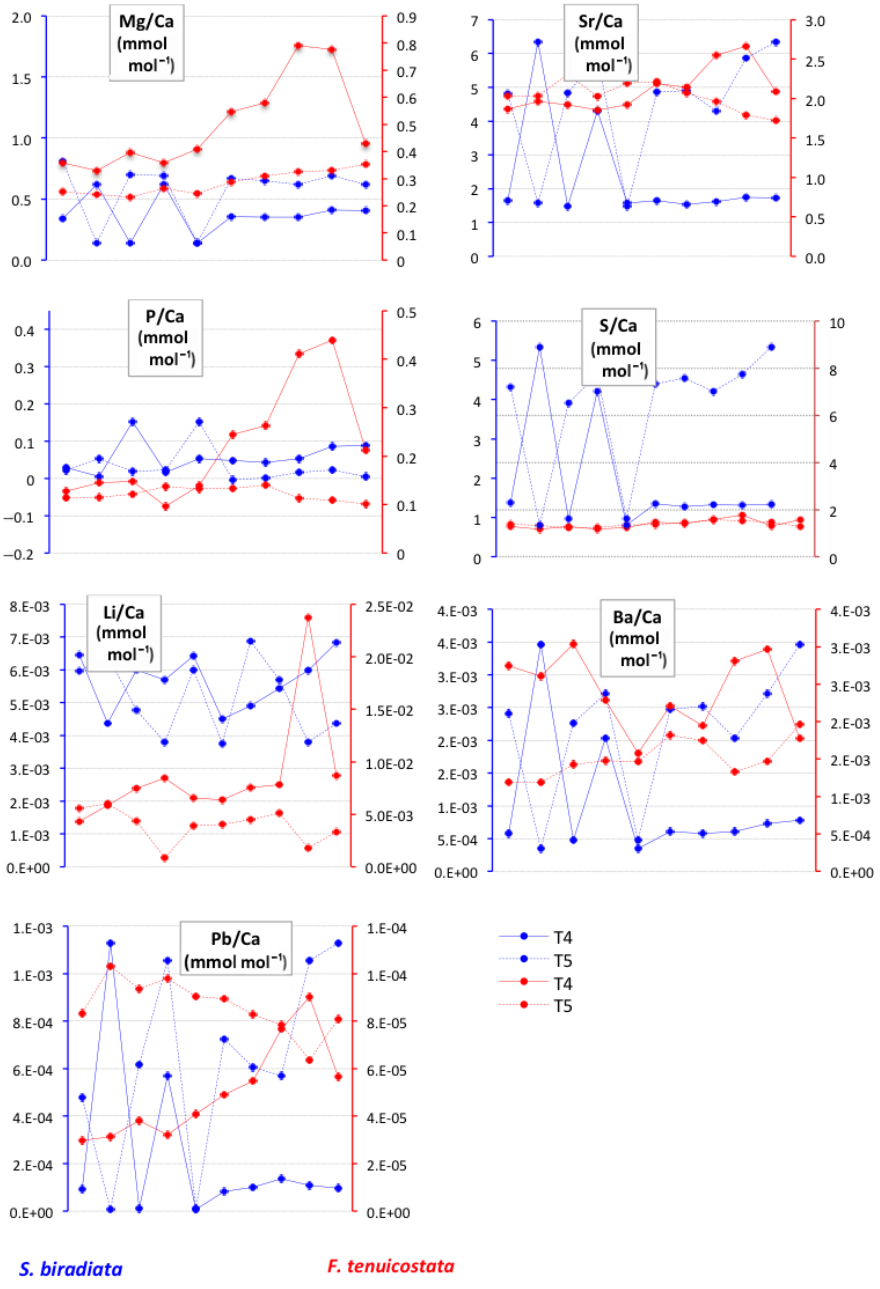

Figure 11. The LA-ICP-MS results for the T4 and T5 transects. The blue lines represent the results for *S. biradiata* (G171) and the red lines represent the results for *F. tenuicostata* (G155).

tion of the shell. For example, Paquette and Reeder (1995) suggested that crystal surface structure has an effect on trace element incorporation. As such, the different microstructures present in the two species studied here may be expected to yield different elemental compositions.

The measured lattice parameters reveal lattice distortion in both *F. tenuicostata* and *S. biradiata* compared to mineral $CaCO_3$. Pokroy et al. (2006) also reported lattice distortions (*Perna canaliculus*, *Acanthocardia tuberculata* and *Strombus decorus*). After lattice parameter permutation, stretching was found along the *a* and *b* axes in both species, and shrinking was found along the *c* axis in *S. biradiata* but not in *F. tenuicostata*. The distortion was not as pronounced in *S. biradiatata* and *F. tenuicostata* compared to the species studied by Pokroy et al. (2006), which can be explained by the use of annealing to relax the $CaCO_3$ structure. The maximum anisotropic distortion in aragonite is $\Delta a/a$ 1.1×10^{-3}, $\Delta b/b$ 2.5×10^{-4} and $\Delta c/c$ 3×10^{-4} for *F. tenuicostata*, and $\Delta a/a$ 1.7×10^{-3}, $\Delta b/b$ 7×10^{-4} and $\Delta c/c$ -6×10^{-4} for *S. biradiata*. According to Pokroy et al. (2006), the organic molecules

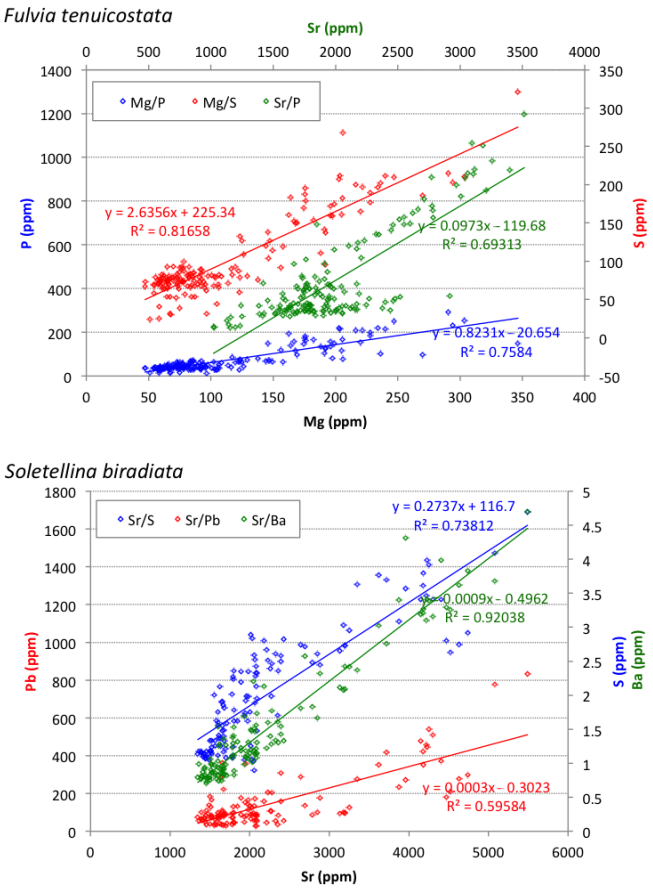

Figure 12. Graphs showing the significant linear correlations of the LA-ICP-MS measurements for *F. tenuicostata* (Mg / P, Mg / S and Sr / P) and *S. biradiata* (Sr / S, Sr / Pb and Sr / Ba).

could be the source of these structural distortions. However, given that the *F. tenuicostata* lattice is more stretched than that of *S. biradiata*, the substitution of Ca^{2+} ions by Mg^{2+} ions described previously could also be a source of distortions. Ion substitution, which has been measured here using XRD, could also be a cause of this distortion because crystal structures accommodate trace elements through dilation or contraction of the ionic site (structural relaxation), which is a factor in the flexibility and stability of the surrounding structure (Finch and Allison, 2007; Loste et al., 2003).

4.2 Chemical composition

The LA-ICP-MS results show that Mg is positively correlated to both S and P, as is Sr to P in *F. tenuicostata*. These Mg correlations are not evident for *S. biradiata*, but Sr is positively correlated to S, Ba and Pb (Fig. 12), as is Ba to S in this latter species.

The strong correlations found in the present study seem to indicate that Mg incorporation is influenced by both phosphorus- and sulfur-containing macromolecules, i.e. both soluble and insoluble fractions of the organic shell matrix in *F. tenuicostata* but not in *S. biradiata*. The incorporation of Sr appears to be influenced by the insoluble fraction of the organic matrix in *S. biradiata* and the soluble fraction in *F. tenuicostata*. The correlation found between Ba and S also suggests that the insoluble organic matrix influences the incorporation of Ba in *S. biradiata*. Shirai et al. (2014) suggested that the incorporation of Sr is highly biologically mediated based on the strong correlation between Sr / Ca, S / Ca and the shell microstructure and that the elemental composition varies at a scale comparable to that of crystallites, i.e. the micrometre scale. The relatively coarse resolution used for LA-ICP-MS (75 µm) does not allow us to verify the spatial scale (< 10 µm) at which the elemental composition of *F. tenuicostata* and *S. biradiata* varies, but we can differentiate between the types of organic macromolecules influencing the shell geochemical composition, i.e. S-dominated or P-dominated. Our findings agree with those of Shirai et al. (2014) in that changes in the microstructure and the S / Ca ratio reflect changes in the organic composition at the mineralisation front. Our findings further show that P / Ca also reflects compositional changes at the mineralisation front. Consequently, we can say that not only do the organic matrices at the calcification front impact the chemical composition of the shell, but its composition also impacts the incorporation of trace elements in the shell, regardless of whether it is S- or P-dominated. This result is consistent with a number of previous studies showing that S-containing and P-containing macromolecules of the shell matrix, insoluble and soluble, respectively, influence nucleation, growth and crystal structure (e.g. Borbas et al., 1991; Crenshaw, 1982; Reddy, 1977; Wheeler and Sikes, 1984). In the context of geochemical proxies, it becomes evident that the combined effects of the shell organic matrix composition and the environmental parameters (e.g. SST) may cause variation in the Mg / Ca and Sr / Ca ratios, two of the most common proxies used for reconstructing paleo-SST.

Additional complexity is also evident. P and S concentrations are consistent (compare the transects of T1, T2 and T3) in *F. tenuicostata* but highly variable in *S. biradiata*. In the latter, low Mg corresponds to high P and S, and high Sr to high S and low P. This suggests that the incorporation of these elements within the shell of *F. tenuicostata* is predominantly influenced by seawater, particularly Mg. In *S. biradiata*, it is predominantly influenced by the organic matrix composition, as demonstrated by the strong correlations in the elements related to the organic matrix. The fact that *S. biradiata* is visibly richer in the organic matrix and owes its strength to its organic fraction, whereas *F. tenuicostata* shells have a thicker and more complex structure (e.g. ridges), might be one explanation for this finding. Another remarkable point of comparison that might help in understanding the differences between the two species of interest lies in their taxonomy. Indeed, both species belong to the Heterodonta subclass and the Cardiida order, but they belong to different superfamilies: Cardioidea and Tellinoidea for *F. tenuicostata*

and *S. biradiata*, respectively (Ponder and Lindberg, 2008). Different organic content and shell organic matrix composition might be explained by evolved differences in the mineralisation processes (Cuif et al., 2011). However, without quantifying organic matrix components (total, soluble and insoluble) and identifying its composition, this remains speculative.

These results not only reinforce the knowledge that the shell organic matrix of bivalves is involved in biomineralisation, but also that its level of influence depends on its composition (phosphorus-containing or sulfur-containing macromolecules) and the specific element being incorporated into the $CaCO_3$. Furthermore, these results show that this phenomenon is species specific. The incorporation of the main elements (e.g. Mg, Sr and Ba) used as proxies from marine properties (e.g. SST) is highly mediated by the shell organic matrix in general.

5 Conclusions

The combination of geochemical, spectroscopic and crystallographic analyses on specimens of *F. tenuicostata* and *S. biradiata* from King George Sound (south Western Australia) has revealed compositional and microstructural differences. Although the specimens were sampled from the same location and experienced the same marine conditions during their growth, they display different characteristics. Both species have been described as purely aragonitic, but low levels of calcite and Mg-calcite are present in *S. biradiata* and *F. tenuicostata*, respectively. The LA-ICP-MS measurements revealed correlations between levels of Mg, S and P (*F. tenuicostata*) and Sr, S and Ba (*S. biradiata*). Although analysing the composition of the shell organic matrix was beyond the scope of this study, the organic matrices of both bivalve species differ in composition and consequently in the way trace elements are incorporated into the $CaCO_3$. The incorporation of Sr and Ba is affected by the S-containing matrix of *S. biradiata*, and the incorporation of Mg and Sr in *F. tenuicostata* is more influenced by S- and P-containing organic macromolecules. The substitution of Ca^{2+} by Mg^{2+} in calcite in *F. tenuicostata* appears to be influenced by the composition of the organic matrix. The combination of S- and P-containing organics could be promoting ionic substitution in the shells of *F. tenuicostata*.

The differences between these two species are clear and raise questions about genetic determinism, considering they belong to different taxonomic superfamilies. This has consequences for environmental proxy applications. The present study shows that the elemental composition of marine bivalve shells is species specific and influenced by multiple factors, such as crystallographic structures, organic macromolecule composition and environmental setting. These factors complicate the use of bivalve shells as a proxy for reconstructing the past and present properties of seawater. Mg / Ca and Sr / Ca ratios are amongst the most common proxies used for SST reconstructions; however, this study shows that the elemental changes are not solely caused by SST variation. The high definition multimodal and multidisciplinary characterisation of both the organic composition and the microstructure are central to understanding calcification and elemental incorporation. Only then can geochemical proxies be used to reconstruct true time series and the "vital effect" accurately described.

Data availability. The data in this paper form part of the PhD research of Liza M. Roger, which has not yet been submitted for examination. The thesis and all data generated as part of the thesis work will be available in the UWA thesis repository after examination.

The Supplement related to this article is available online at doi:10.5194/bg-14-1721-2017-supplement.

Author contributions. Liza M. Roger wrote the paper, collected the samples and analysed them. As PhD supervisors, Annette D. George and Jeremy Shaw supervised the research and reviewed the paper. Robert D. Hart helped with the understanding and analysis of the XRD data. Malcolm Roberts collected the EPMA data. Thomas Becker helped with the understanding of the CRM data. Bradley J. McDonald and Noreen J. Evans collected the LA-ICP-MS data.

Competing interests. The authors declare that they have no conflict of interest.

Disclaimer. This paper is the result of the analyses that form part of the PhD research of Liza M. Roger at the University of Western Australia and the Centre for Microanalysis, Characterisation and Analysis in collaboration with the John de Laeter Centre of Curtin University; it is subject to interpretation.

Acknowledgements. The authors acknowledge the facilities and the scientific and technical assistance of the Australian Microscopy abnd Microanalysis Research Facility at the Centre for Microscopy, Characterisation and Analysis at the University of Western Australia; this is a facility funded by the university, state and commonwealth governments and the John de Laeter Centre at Curtin University, which is a GeoHistory Facility and collaborative research venture involving Curtin University, the University of Western Australia, the Geological Survey of Western Australia and the Commonwealth Scientific and Industrial Research Organisation (CSIRO). The authors are also grateful for the constructive comments and notes provided by B. Schöne and the technical assistance provided by F. Nemeth. This study was financially

supported by the School of Earth Sciences and the Centre for Microscopy, Characterisation and Analysis of the University of Western Australia.

Edited by: H. Kitazato
Reviewed by: A. D. Wanamaker Jr. and two anonymous referees

References

Armstrong, J. T.: Quantitative analysis of silicate and oxide minerals: Comparison of Monte-Carlo, ZAF and Phi-Rho-Z procedures, San Francisco Press, San Francisco, 1988.

Ayling, B. F., Chappell, J., McCulloch, M. T., Gagan, M. K., and Elliot, M.: High-resolution paleoclimate of the MIS 11 interglacial (423–360 ka) using geochemical proxies in giant *Tridacna* clams, Geochim. Cosmochim. Ac., 70, A26, doi:10.1016/j.gca.2006.06.066, 2006.

Bonham, K.: Growth Rate of Giant Clam *Tridacna gigas* at Bikini Atoll as Revealed by Radioautography, Science, 149, 300–302, doi:10.1126/science.149.3681.300, 1965.

Borbas, J. E., Wheeler, A. P., and Sikes, C. S.: Molluscan shell matrix phorphoroproteins: correlation of degree of phosphorylation to shell mineral microstructure and to in vitro regulation of mineralization, J. Exp. Zool., 258, 1–13, 1991.

Bowerbank, J. S.: On the structure of the shells of molluscan and conchyferous animals, Trans. Microsc. Soc. London, 1, 123–152, 1844.

Bragg, W. L.: Zeitschrift fur Kristallographie, Kristallgeometrie, Kristallphysik, Kristallchemie (-144, 1977), 61, 425–452, 1925.

Brouwers, N. C., Mercer, J., Lyons, T., Poot, P., Veneklaas, E., and Hardy, G.: Climate and landscape drivers of tree decline in a Mediterranean ecoregion, Ecology and Evolution, 2013, 67–79, 2013.

Carpenter, W.: On the microscopic structure of shells: Part I., Br. Assoc. Adv. Sci., 14, 1–24, 1845.

Carpenter, W.: On the microscopic structure of shells: Part II., Br. Assoc. Adv. Sci., 17, 93–134, 1847.

Carré, M., Bentaleb, I., Bruguier, O., Ordinola, E., Barrett, N. T., and Fontugne, M.: Calcification rate influence on trace element concentrations in aragonitic bivalve shells: Evidences and mechanisms, Geochim. Cosmochim. Ac., 70, 4906–4920, 2006.

Crenshaw, M. A.: Biological mineralization and demineralization, Springer, Berlin Heidelberg, 1982.

Cresswell, G. R. and Golding, T. J.: Observations of a south-flowing current in the southeastern Indian Ocean, Deep-Sea Res., 27A, 449–466, 1980.

Cuif, J. P., Dauphin, Y., and Sorauf, J. E.: Biominerals and Fossils Through Time, Cambridge University Press, Cambridge, 2011.

Cuif, J. P., Dauphin, Y., Nehrke, G., Nouet, J., and Perez-Huerta, A.: Layered growth and crystallization in calcareous biominerals: impact of structureal and chemical evidence on two major concepts in invertebrate biomineralization studies, Minerals, 2, 11–39, 2012.

Cullity, B. D. and Weymouth, J. W.: Elements of X-ray diffraction, Am. J. Phys., 25, 394–395, 1957.

De Villiers, J. P. R.: The crystal structures of aragonite, strontianite and witherite, PhD Diss., University of Illinois at Urbana-Champaign, 1967.

Donovan, J. J. and Tingle, T. N.: An improved mean atomic number correction for quantitative microanalysis, J. Microsc., 2, 1–7, 1996.

Ferguson, J. E., Henderson, G. M., Fa, D. A., Finlayson, J. C., and Charnley, N. R.: Increased seasonality in the Western Mediterranean during the last glacial from limpet shell geochemistry, Earth Planet. Sc. Lett., 308, 325–333, 2011.

Finch, A. A. and Allison, N.: Coordination of Sr and Mg in calcite and aragonite, Mineral. Mag., 71, 539–552, 2007.

Freitas, P. S., Clarke, L. J., Kennedy, H., Richardson, C. A., and Abrantes, F.: Environmental and biological controls on elemental (Mg / Ca, Sr / Ca and Mn/Ca) ratios in shells of the king scallop *Pecten maximus*, Geochim. Cosmochim. Ac., 70, 5119–5133, 2006.

Gattuso, J. P. and Hansson, L.: Ocean Acidification, Oxford Univeristy Press, New York, 2011.

Gazeau, F., Gattuso, J.-P., Dawber, C., Pronker, A. E., Peene, F., Peene, J., Heip, C. H. R., and Middelburg, J. J.: Effect of ocean acidification on the early life stages of the blue mussel *Mytilus edulis*, Biogeosciences, 7, 2051–2060, doi:10.5194/bg-7-2051-2010, 2010.

Gillikin, D. P., De Ridder, F., Ulens, H., Elskens, M., Keppens, E., Baeyens, W., and Dehairs, F.: Assessing the reproducibility and reliability of estuarine bivalve shells (*Saxidomus giganteus*) for sea surface temperature reconstruction: implications for paleoclimate studies, Paleogeogr. Paleocl., 228, 70–85, 2005a.

Gillikin, D. P., Lorrain, A., Navez, J., Taylor, J. W., Keppens, E., Baeyens, W., and Dehairs, F.: Strong biological controls on Sr / Ca ratios in aragonite marine bivalve shells, Geochem. Geophy., Geosy., 6, Q05009, doi:10.1029/2004GC000874, 2005b.

Hahn, S., Griesshaber, E., Schmahl, W. W., Neuser, R. D., Ritter, A.-C., Hoffmann, R., Buhl, D., Niedermayr, A., Geske, A., Immenhauser, A., and Pufahl, P.: Exploring aberrant bivalve shell ultrastructure and geochemistry as proxies for past sea water acidification, Sedimentology, 61, 1625–1658, doi:10.1111/sed.12107, 2014.

Heinemann, A.: The suitability of Mytilus edulis as proxy archive and its response to ocean acidification, PhD, Christian-Albrechts-Universität, Kiel, Germany, 2011.

Henkes, G. A., Passey, B. H., Wanamaker, A. D., Grossman, E. L., Ambrose, W. G., and Carroll, M. L.: Carbonate clumped isotope compositions of modern marine mollusk and brachiopod shells, Geochim. Cosmochim. Ac., 106, 307–325, 2013.

Jacob, D. E., Soldati, A. L., Wirth, R., Huth, J., Wehrmeister, U., and Hofmeister, W.: Nanostructure, composition and mechanisms of bivalve shell growth, Geochim. Cosmochim. Ac., 72, 5401–5415, 2008.

Jones, D. S. and Quitmyer, I. R.: Marking time with bivalve shells: oxygen isotopes and season of annual increment formation, Palaios, 11, 340–346, 1996.

Klausmeyer, K. R. and Shaw, M. R.: Climate change, habitat loss, protected areas and the climate adaptation potential of species in Mediterranean ecosystems worldwide, PloS one, 4, e6392, doi:10.1371/journal.pone.0006392, 2009.

Klein, R. T., Lohmann, K. C., and Thayer, C. W.: Sr / Ca and ^{13}C / ^{12}C ratios in skeletal calcite of *Mytilus trossulus* : covariation with metabolic rate, salinity and carbon isotopic composition of seawater, Geochim. Cosmochim. Ac., 60, 4207–4221, 1996.

Krause-Nehring, J., Klùgel, A., Nehrke, G., Brellochs, B., and Brey, T.: Impact of sample pretreatment on the measured element concentrations in the bivalve *Arctica islandica*, Geochem. Geophy. Geosy., 12, 1525–2027, 2011.

Lazareth, C. E., Putten, E. V., André, L., and Dehairs, F.: High-resolution trace element profiles in shells of the mangrove bivalve *Isognomon ephippium*:a record of environmental spatio-temporal variations, Estuar. Coast. Shelf S., 57, 1103–1114, 2003.

Lazareth, C. E., Le Cornec, F., Candaudap, F., and Freydier, R.: Trace element heterogeneity along isochronous growth layers in bivalve shell: Consequences for environmental reconstruction, Palaeogeogr. Palaeocl., 373, 39–49, 2013.

Loste, E., Wilson, R. M., Seshadri, R., and Meldrum, F. C.: The role of magnesium in stabilising amorphous calcium carbonate and controlling calcite morphologies, J. Cryst. Growth, 254, 206–218, 2003.

Lowenstam, H. A. and Weiner, S.: On Biomineralization, New York, Oxford, 1989.

Mucci, A. and Morse, J. W.: The incorporation of Mg^{2+} and Sr^{2+} into calcite overgrowths: influences of growth rate and solution composition, Geochim. Cosmochim. Ac., 47, 217–233, 1982.

Nategaal, R., Grove, C. A., Kasper, S., Zinke, J., Boer, W., and Brummer, G.-J. A.: Spectral luminescence and geochemistry of coral aragonite: effects of whole-core treatment, Chem. Geol., 318–319, 6–15, 2012.

Nehrke, G. and Nouet, J.: Confocal Raman microscope mapping as a tool to describe different mineral and organic phases at high spatial resolution within marine biogenic carbonates: case study on *Nerita undata* (Gastropoda, Neritopsina), Biogeosciences, 8, 3761–3769, doi:10.5194/bg-8-3761-2011, 2011.

Paquette, J. and Reeder, R. J.: Relationship between surface structure, growth mechanism, and trace element incorporation in calcite, Geochim. Cosmochim. Ac., 59, 735–749, 1995.

Pokroy, B., Fitch, A. N., Lee, P. L., Quintana, J. P., Caspi, E. N., and Zolotoyabko, E.: Anisotropic lattice distortions in the mollusk-made aragonite: a widespread phenomenon, J. Struct. Biol. , 153, 145–150, 2006.

Pokroy, B., Fieramosca, J. S., Von Dreele, R. B., Fitch, A. N., Caspi, E. N., and Zolotoyabko, E.: Atomic structure of biogenic aragonite, Chem. Mater., 10, 3244–3251 doi:10.1021/cm070187u, 2007.

Popov, S. J.: Composite prismatic structures in bivalve shell, Acta Palaeontologica Polonica, 31, 3–26, 1986.

Ponder, W. F. and Lindberg, D. R.: Phylogeny and Evolution of the Mollusca, University of California Press, London, 2008.

Purton, L. M. A., Sheilds, G. A., Brasier, M. D., and Grime, G. W.: Metabolism controls Sr / Ca ratios in fossil aragonite molluscs, Geology, 27, 1083–1086, 1999.

Reddy, M. M.: Crystallization of calcium carbonate in the presence of trace concentrations of phosphorus-containing anions: I. Inhibition by phosphate and glycerophsphate ions at pH 8.8 and 25 C, J. Cryst. Growth, 41, 287–295, 1977.

Richardson, C. A., Peharda, M., Kennedy, H., Kennedy, P., and Onofri, V.: Age, growth rate and season of recruitment of *Pinna nobilis* (L) in the Croatian Adriatic determined from Mg : Ca and Sr : Ca shell profiles, J. Exp. Mar. Biol. Ecol., 299, 1–16, 2004.

Scarlett, N. V. Y. and Madsen, I. C.: Quantification of phases with partial or no known crystal structures, Powder Diffraction, 21, 278–284, 2006.

Schneider, J. A. and Carter, J. G.: Evolution and phylogenetic significance of Cardioidean shell microstructure (Mollusca, Bivalvia), J. Paleontol., 75, 607–643, 2001.

Schöne, B. R., Dunca, E., Mutvei, H., and Norlund, U.: A 217-year recorad of summer air temperature reconstructed from freshwater pearl mussels (*M. margaritifera*, Sweden), Quaternary Sci. Rev., 23, 1803–1816, 2004.

Schöne, B. R., Houk, S. D., Castro, A. D. F., Fiebig, J., Oschmann, W., Kroncke, I., Dreyer, W., and Gosselck, F.: Daily growth rates in shells of *Arctica islandica*: Assessing sub-seasonal environmental controls on a long-lived bivalve mollusk, Palaios, 20, 78–92, 2005.

Schöne, B. R., Zhang, Z., Jacob, D. E., Gillikin, D. P., Tutken, T., Garbe-Schönberg, D., McConnaughey, T. A., and Soldati, A. L.: Effect of organic matrices on the determination of the trace element chemistry (Mg, Sr, Mg / Ca, Sr / Ca) of aragonite bivalve shells (*Arctica islandica)* – Comparison of ICP-OES and LA-ICP-MS data, Geochem. J., 44, 23–37, 2010.

Schöne, B. R., Zhang, Z., Radermacher, P., Thébault, J., Jacob, D. E., Nunn, E. V., and Maurer, A.-F.: Sr / Ca and Mg / Ca ratios of ontogenetically old, long-lived bivalve shells (*Arctica islandica*) and their function as paleotemperature proxies, Palaeogeogr. Palaeocl., 302, 52–64, 2011.

Schöne, B. R., Radermacher, P., Zhang, Z., and Jacob, D. E.: Crystal fabrics and element impurities (Sr / Ca, Mg / Ca, and Ba / Ca) in shells of *Arctica islandica* – Implications for paleoclimate reconstructions, Palaeogeogr. Palaeocl., 373, 50–59, 2013.

Schroeder, J. H., Dwornik, E. J., and Papike, J. J.: Primary Protodolomite in Echinoid Skeleton, Geol. Soc. Am. Bull., 80, 1613–1616, 1969.

Shirai, K., Schöne, B. R., Miyaji, T., Radarmacher, P., Krause, R. A., and Tanabe, K.: Assessment of the mechanism of elemental incorporation into bivalve shells (*Arctica islandica*) based on elemental distribution at the microstructural scale, Geochim. Cosmochim. Ac., 126, 307–320, 2014.

Spero, H. J., Lerche, I., and Williams, D. F.: Opening the carbon isotope "vital effect" black box, 2, quantitative model for interpreting foraminiferal carbon isotope data, Paleoceanography, 6, 639–655, 1991.

Strom, A., Francis, R. C., Mantua, N. J., Miles, E. L., and Peterson, D. L.: North Pacific climate recorded in growth rings of geoduck clams; a new tool for paleoenvironmental reconstruction, Geophys. Res. Lett., 31, L06206, doi:10.1029/2004GL019440, 2004.

Takesue, R. K., Bacon, C. R., and Thompson, J. K.: Influences of organic matter and calcification rate on trace elements in aragonitic estuarine bivalve shells, Geochim. Cosmochim. Ac., 72, 5431–5445, 2008.

Urey, H. C., Lowenstam, H. A., Epstein, A. W., and McKinney, C. R.: Measurement of paleotemperatures and temperatures of the Upper Creataceaous of England, Denmark, and the Southeastern United States, Bull. Geol. Soc. Am., 62, 399–416, 1951.

Wanamaker, A. D., Hetzinger, S., and Halfar, J.: Reconstructing mid- to high-latitude marine climate and ocean variability using bivalves, coralline algae, and marine sediment cores from the Northern Hemisphere, Palaeogeogr. Palaeocl., 302, 1–9, 2011.

Wheeler, A. P. and Sikes, C. S.: Regulation of carbonate calcification by organic matrix, Am. Zool., 24, 933–944, 1984.

WoRMS Editorial Board: World Register of Marine Species, available at: http://www.marinespecies.org (last access: 26 October 2016), doi:10.14284/170, 2016.

Zeebe, R., Bijma, J., Hönisch, B., Sanyal, A., Spero, H. J., and Wolf-Gladrow, D. A.: Vital effects and beyond: a modelling perspective on developing paleoceanographical proxy relationships in foraminifera, Geol. Soc., London, Special Publications, 303, 45–58, 2008.